Medicine in Novel Technology and Devices 3 (2019) 100020

Contents lists available at ScienceDirect

Medicine in Novel Technology and Devices

journal homepage: www.journals.elsevier.com/medicine-in-novel-technology-and-devices/

Research Paper

The role of porosity and 3D cross-stent configuration of multiple overlapping uncovered stents in the management of complex aortic aneurysms – Insights from haemodynamics

Shuo Wang [a,1], Yongxue Zhang [b,1], Jianxuan Feng [b], Yuan Huang [c], Pinjing Hui [d], Jonathan H. Gillard [a], Qingsheng Lu [b,**], Zhongzhao Teng [a,e,f,*]

[a] Department of Radiology, University of Cambridge, UK
[b] Department of Vascular Surgery, Changhai Hospital, Shanghai, China
[c] EPSRC Centre for Mathematical and Statistical Analysis of Multimodal Clinical Imaging, University of Cambridge, UK
[d] Department of Stroke Center, The First Affiliated Hospital of Soochow University, Suzhou, China
[e] Department of Engineering, University of Cambridge, UK
[f] Beijing Advanced Innovation Center for Biomedical Engineering, Beihang University, Beijing, China

ARTICLE INFO

Keywords:
Aortic aneurysm
Bare metal stent
Branch
Porosity
Mechanics

ABSTRACT

Background: Multiple overlapping uncovered stents (MOUS) have been introduced to manage complex aortic aneurysms with vital branches involvement. It has been shown that the porosity is a key determinant of the treatment outcome. However, the role of 3D cross-stent configuration remains unclear.

Methods: One patient with a complex aortic aneurysm judged not suitable for open surgery nor endovascular repair was invited to participate this study. In total, four bare metal stents were deployed. 3D lesion geometry was reconstructed based on pre- and post-operative CTA, and the zero-pressure configuration was recovered using an inverse procedure. Local haemodynamic parameters, including wall shear stress (WSS), oscillatory shear index (OSI), and particle relative resident time (RRT), as well as the vessel structural stress (VSS), were quantified using one-way fluid-structure interaction (FSI) analysis. In comparison to MOUS, a corresponding compact model was reconstructed by projecting inner layer stents to the most outer layer to form a single layer to eliminate the 3D cross-stent configuration and one-way FSI analysis was performed.

Results: Results obtained showed that the porosity decreased linearly with the number of stents. When the 1st stent was deployed, the mean velocity decreased 36.4% and further reduction of 49.3%, 59.8%, and 62.8% were observed when the 2nd, 3rd and 4th stents were deployed. WSS also decreased with the number of stents deployed, and both OSI and RRT increased, but the increase was very minor with the 4th stent. MOUS deployment induced high VSS concentration in the landing zone while the VSS and pressure in the sac remained nearly unchanged. The compact model yielded a small difference in the value of flow-related parameters and 10%–20% reduction in VSS.

Conclusion: Compared with porosity, the 3D cross-stent of MOUS configuration plays a minor role in the modulation of local haemodynamics. A compact model does not reduce high VSS concentration in the diseased region significantly.

1. Introduction

Flow diverters were firstly introduced to treat intracranial aneurysms. In the early 1990s, a stent-like endoprosthesis was used to treat experimental carotid artery aneurysms in animal models and successfully excluded the lesion from circulation [1]. A stent-assisted coiling

* Corresponding author. University Department of Radiology, University of Cambridge, Level 5, Box 218, Addenbrooke's Hospital, Hills Rd., Cambridge, CB2 0QQ, UK.
** Corresponding author. Division of Vascular Surgery, Changhai Hospital, 168 Changhai Road, 200433, Shanghai, China.
E-mail addresses: luqs@xueguan.net (Q. Lu), zt215@cam.ac.uk (Z. Teng).
[1] Equal authorship.

https://doi.org/10.1016/j.medntd.2019.100020
Received 2 September 2019; Received in revised form 14 November 2019; Accepted 25 November 2019

procedure was reported in 1997 for a ruptured fusiform vertebrobasilar artery aneurysm [2] and the first clinical use of a flow diverter in North America was reported in 2008 [3]. Further technical developments have improved the cure rate and lowered complication rates. This technique has transformed the management of intracranial aneurysms, becoming the preferred treatment option for large or giant wide-necked lesions [4].

Flow diverter harnesses the blood rheological properties by altering blood flow, and induces thrombosis formation within the sac [5]. The formation of mural thrombus increases the effective wall thickness and decreases the lumen radius, and therefore reduces the aneurysm wall tension and the risk of aneurysm rupture [6]. A major advantage of this technology is its capacity to keep long-term patency of side branches [7]. Porosity has been shown to be one of the determinants for an optimal treatment effect and a porosity of 50%–70% is reported to be ideal for the intracranial aneurysm occlusion [8,9].

Encouraged by the success in treating intracranial aneurysms, researchers have attempted to manage complex aortic aneurysms with subbranches involvement using multiple overlapping uncovered stents (MOUS)[10,11]. Compared with the intracranial circulation, the aortic aneurysm is a more challenging territory for MOUS due to its complex haemodynamics environment, e.g., large lesion size and much higher flow velocity [12]. Moreover, the porosity, the shape of cells enclosed by the stent beams and the cross stents configuration vary a lot when more than one stent is deployed. Virtual deployments following Monto Carlo procedure showed that the porosity decreases linearly with the number of stents deployed, e.g., the mesh porosity is 85.2% for a single-layer OptiMed stent (Ettlingen, Germany), and it drops to 72.2%, 60.5% and 52.4% for two, three, and four stents, respectively. It has been reported that on average 3.3 stents are needed for one aortic aneurysm [10]. It has also been demonstrated that as long as there is misalignment between stents either in the circumferential or axial direction, the percentage of flow velocity reduction was not affected [13].

However, in addition to 2D overlapping patterns, the deployment of multiple stents also generates 3D cross-stent structure in the radial direction. The role of such 3D cross-stent configuration in modulating the local flow pattern still remains unclear. To investigate the role of cross-stent structure, a compact model of one single layer was built by projecting inner stents outwards to the surface of the outmost stent. The change of local haemodynamics was studied by comparing models with and without projection.

2. Materials and methods

2.1. The patient information

Data used in this study is from one of patients reported previously [10,13] and was approved by the review board of Changhai Hospital, Shanghai, China. This patient was a 68-year-old male, with a complex thoracoabdominal aortic aneurysm (maximum diameter, 70.1 mm) (Fig. 1A). Medical history included pulmonary function impairment, grade II hypertension (146/92 mmHg, heart rate 68 bpm) and coronary artery disease that had been previously treated by stenting. Given his multiple comorbid conditions and the risk of spinal cord ischaemia (at the level of T11-L1) and occlusion of coeliac arteries if stent-graft was used, the patient was judged unsuitable for either open surgery or traditional endovascular repair by a multidisciplinary team consisting of

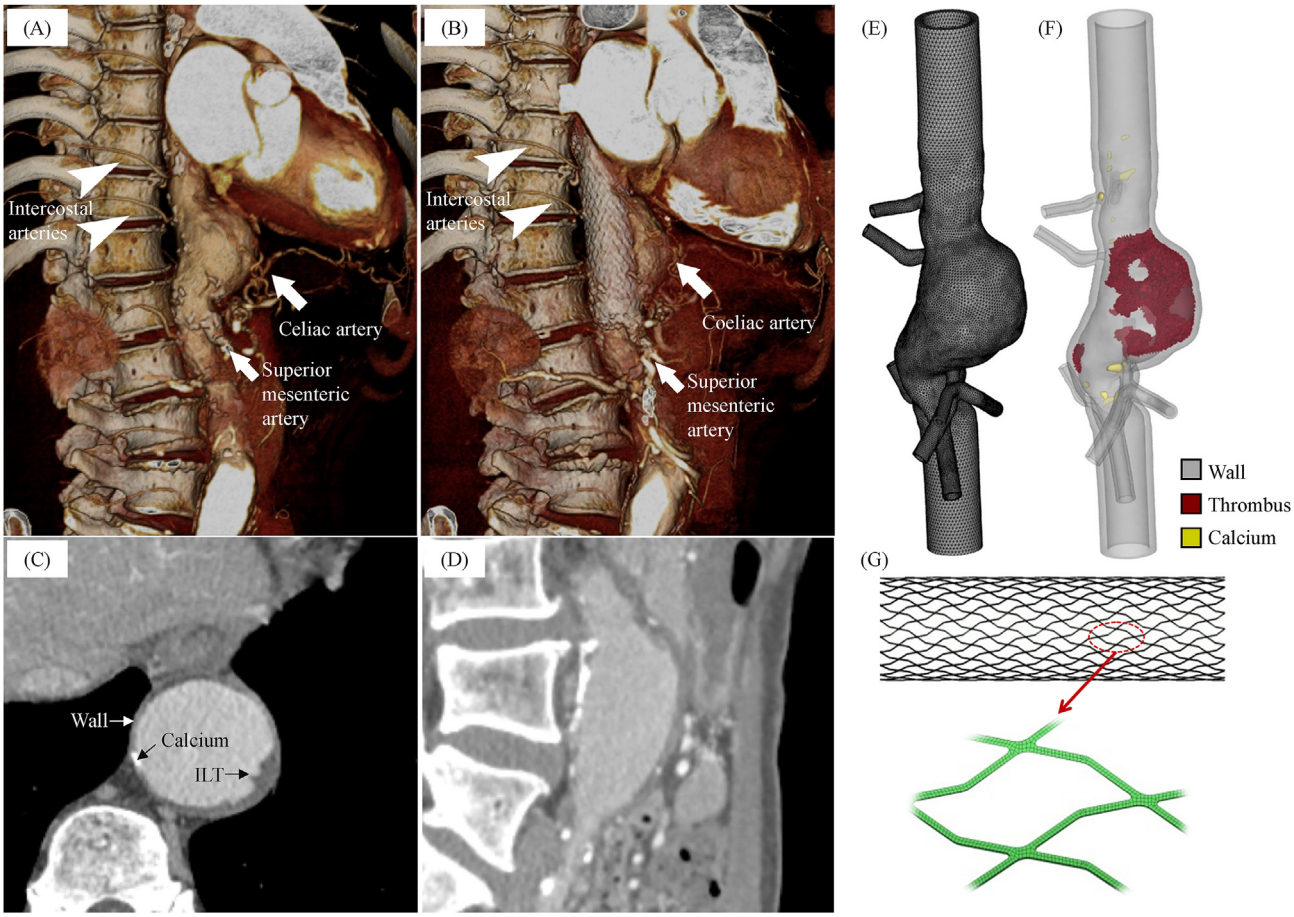

Fig. 1. The configuration of a complex aortic aneurysm with vital branches involvement. (A) 3D rendering of the lesion configuration before stent deployment; (B) 3D rendering of the configuration after 4-layer stents deployment; (C) A 2D axial CTA slice; (D) A 2D sagittal CTA slice; (E) Reconstructed 3D geometry with mesh; (F) Sagittal cut showing intraluminal thrombus and calcium; (G) 3D stent model with mesh.

vascular surgeons, cardio-thoracic surgeons, and anaesthetists. The MOUS strategy was therefore suggested to the patient, who gave written informed consent (Fig. 1B). Closed-cell, self-expandable and uncovered sinus-XL stents from OptiMed (Ettlingen, Germany) were used (Fig. 1G). The diameter and length of the uncovered stents deployed in this patient were 28 mm and 100 mm, respectively.

2.2. Stent and aneurysm geometry reconstruction and meshing

The geometry of the bare metal stent was reconstructed according to the parameters provided by the supplier in Creo2.0 (PTC, Needham, USA) (Fig. 1G). The stent was meshed in ICEM (ANSYS Inc., PA, USA). A single stent was meshed with 119,592 hexahedron elements. The typical length of each element was approximately 0.15 mm.

The aneurysm lumen contour, and calcium and thrombus in the lesion were segmented based on the pre-operative contrast-enhanced computed tomography angiology (CTA) images with a resolution of 0.683 × 0.683 × 0.8 mm^3 (Fig. 1C&D) using an in-house program developed in MATLAB R2016a (The MathWorks, Inc., USA) [14]. The aortic wall thickness was about 2.5 mm and the diameters of visible sub-branches ranged from 2.9 mm to 6.0 mm with a ~1.0 mm wall thickness. The segmented contours were translated into a voxel-based label map and resampled with a voxel size of 0.1 × 0.1 × 0.1 mm^3 to reduce the effect from smoothing operation. The map was imported into 3D Slicer (http://www.slicer.org/) and aortic components and sub-branches were merged by Boolean operation and smoothed using the Gaussian Filter.

After completion of the final voxel-based label maps for aneurysm, the surfaces of each object were generated using fast marching method in 3D Slicer and imported to VMTK (http://www.vmtk.org/), followed by smoothing with Taubin's algorithm [15]. Finally, surfaces of inlet and outlet of the aneurysm and the outlet of each sub-branch were clipped and extended 15 times of the local diameter to eliminate the inlet and outlet effect (Fig. 1E). Volumes enclosed by these surfaces were generated, and then meshed with tetrahedral elements based on local curvatures in ICEM (Fig. 1E&F). In the pre-operative model without any stent, 409,357 tetrahedral elements were generated for the solid domain of the aneurysm.

2.3. Fluid-structure interaction analysis

In this study, a one-way fluid-structure interaction (FSI) analysis was performed to calculate the mechanical conditions before and after the MOUS deployment. The influence of stent deployment on critical mechanical conditions was investigated within the aneurysmal structure and blood flow in the sac and side branches was analysed. The workflow can be found in Fig. 2.

- Zero-pressure configuration calculation

The in vivo CTA images were acquired under pressurised condition and the analysis needs to be based on zero-pressure configuration. An inverse procedure with an internal pressure of 110 mmHg (patient's

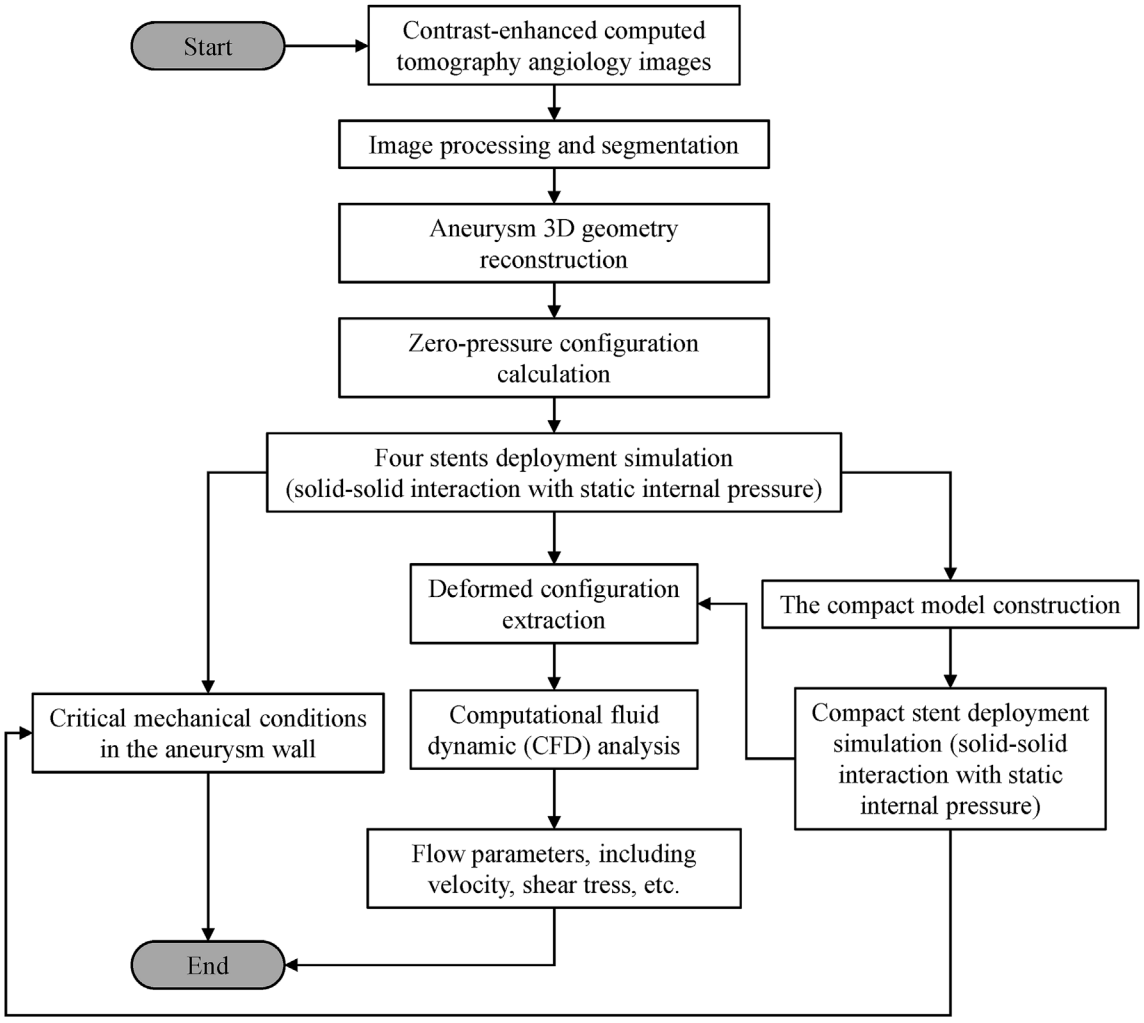

Fig. 2. The workflow of mechanical analysis in this study.

mean blood pressure) and an axial stretch of 2.5% was therefore followed to obtain the computational starting shape [16]. Each stent was assumed to be a linear material with Young's modulus and Poison's ratio of 75 GPa and 0.333, respectively. The modified Mooney-Rivlin model was used to describe the material properties of the aortic wall, thrombus and calcium. The material constants are adapted from the previous experimental results of aortic aneurysm [17,18]: aortic wall, $C_1 = 0.07$ kPa, $D_1 = 6.54$ kPa and $D_2 = 5.88$; thrombus, $C_1 = 0.24$ kPa, $D_1 = 8.69$ kPa and $D_2 = 0.61$; and calcium, $C_1 = 1.15 \times 10^5$ kPa, $D_1 = 7.67 \times 10^4$ kPa, and $D_2 = 2.83 \times 10^{-8}$.

- **Solid-solid interaction analysis**

A static pressure of 110 mmHg (the patient's mean blood pressure) was applied on the luminal surface and an axial stretch of 2.5% was prescribed at both aortic ends to restore the in-vivo configuration. The stents' surface and lumen surface were defined as contact surfaces. Steps mimicking the deployment were as follows: (1) a concentrated force that gradually increased from 0 to 350 N was applied at both ends of the stent along its axial direction to radially shrink the stent; (2) a rigid body displacement was prescribed to deliver the stents into the lumen to the target location, which were identified by the locations of radio-opaque markers on the post-operative CTA images; (3) the stent was released by gradually decreasing the concentrated force to 0. Multiple stents were deployed sequentially controlled by the phase-shifted time functions.

Different degrees of freedom (DOF) fixity policies were adapted to eliminate rigid displacements where appropriate for different parts. The displacement of both ends of the extended aorta was specified to maintain the axial stretch ratio, and circumferential rotation of nodes on these two ends was not allowed. For each side branch, all DOFs at the end were fixed except for the local radial displacement. For stents, circumferential rotation and axial displacement at the proximal (close to the heart) were not allowed, while no constriction for the other end. The virtual deployment simulation was performed using ADINA 9.0 (ADINA Inc., MA, USA) in the implicit statics mode with the consideration of large strain and large displacement. An auto time step technique was used for the consideration of convergence. Finally, averaged and peak von Mises stress was extracted under the 99.5% criterion as the indicator of vessel structural stress (VSS) in the wall.

- **Computational fluid dynamics (CFD) analysis**

The deformed lumen and stent struts surface after deployment were extracted to form the fluid domain (no strut surface in the case without stent deployments). The stent struts in direct contact with the aortic wall were masked out to reduce computational costs. Then the fluid domain was imported into ICEM CFD and meshed using the Octree method with tetrahedral elements (Fig. 3A). The thickness of the boundary layer was estimated to be 1.4 mm considering the Womersley number of ~18.2 in this study. Three prism thin boundary layers were generated for a fine calculation in the region near the lumen surface with the first two layers thickness being 0.4 mm and the third 0.8 mm [19,20]. In total, the fluid

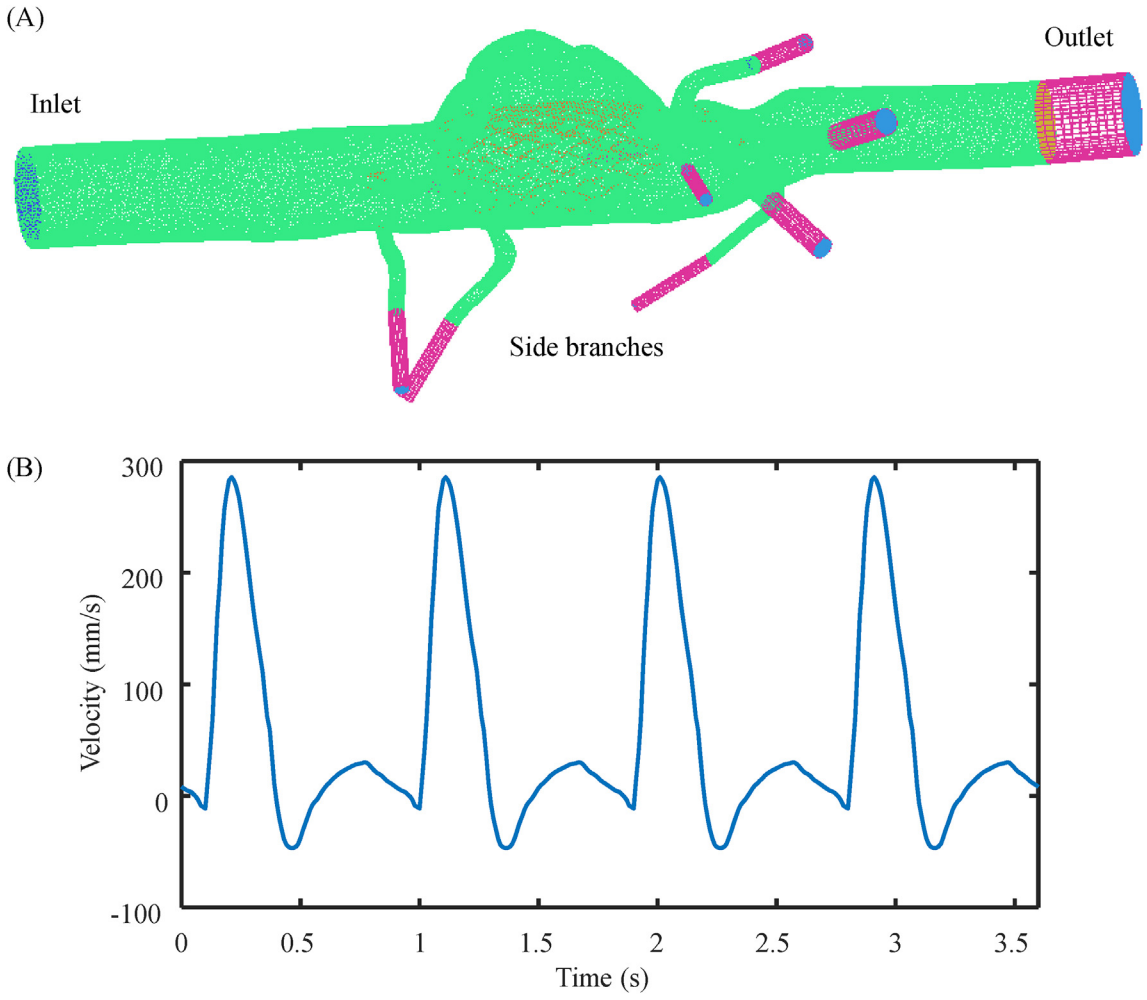

Fig. 3. The mesh of the fluid domain and the velocity waveform at the inlet. (A) The fluid domain was meshed with tetrahedron and prism elements based on the deployed geometry of MOUS. Impendence units are added at the main outlet and end of the side branches (pink); (B) The 'plug' velocity waveform applied at the inlet.

domain without stents was meshed with 80,562 tetrahedral and 175,691 prism elements; a single stent with 518,988 tetrahedral and 99,037 prism elements; two stents with 832,072 tetrahedral and 105,722 prism elements; three stents with 943,176 tetrahedral elements and 114,642 prism elements; and four stents with 1,004,782 tetrahedral elements and 126,128 prism elements.

A 'plug' velocity profile with a mean velocity of 66.7 mm/s and peak velocity 284.0 mm/s was adopted from measurements by Olufsen et al. as the loading conditions at the aortic inlet (Fig. 3B)[21]. At the outlets, a resistant unit was added at each outlet to mimic the afterload of the downstream circulation bed [22]. The resistance of each unit was determined by the following steps: (1) a CFD simulation without resistance units was performed by assigning discharge ratio of each outlet according to Murray's Law [23] and a pressure profile was applied at the outlet of the aorta; and (2) extract computed pressure at the outlet of each side branch and calculate the resistance by *resistance = (mean pressure)/(mean flow rate)*.

The blood was assumed to be incompressible and Newtonian with a density of 1.06 g/cm^3 and a constant viscosity of 0.035 P, and the flow to be transient laminar. The Newton-Raphson iteration method was used for each time step with a convergence criterion for the relative residual of 0.001. Simulation was performed over 4 cardiac cycles. Results of the last cycle were extracted for analysis where the flow was fully developed.

Wall shear stress (WSS)[24,25], oscillatory shear index (OSI) [25] and particle relative resident time (RRT) [26,27] have been widely suggested to be associated with atherosclerosis and aneurysm development and their clinical presentations. With this consideration, apart from flow velocity and rate, these parameters were also used to quantify the flow pattern modulated by the stent deployment. RRT was normalised ($\overline{RRT}$) by the average value in the case before deployment at the proximal disease-free region where the flow was fully developed. WSS can be obtained from the stress tensor $\boldsymbol{\sigma}$,

$$\boldsymbol{\tau}_w(\mathbf{X},t) = \mathbf{n}(\mathbf{X}) \cdot \boldsymbol{\sigma}(\mathbf{X},t) \cdot \mathbf{n}(\mathbf{X})$$

where $\mathbf{n}$ is the normal direction of vessel wall. The time-averaged wall shear stress (TAWSS) is calculated by integrating WSS magnitude over the cardiac cycle,

$$\mathrm{TAWSS} = \frac{1}{T}\int_0^T |\boldsymbol{\tau}_w| dt$$

OSI is a dimensionless metric which characterises whether the WSS vector is aligned with the TAWSS vector throughout the cardiac cycle, defined as,

$$\mathrm{OSI} = \frac{1}{2}\left(1 - \frac{\left|\int_0^T \boldsymbol{\tau}_w \ dt\right|}{\int_0^T |\boldsymbol{\tau}_w| dt}\right)$$

The OSI is greater than zero if there is some direction change during the flow cycle, and the maximum value is 0.5 in the case of pure oscillatory flow without any net forward flow. RRT at a specific site is inversely proportional to the distance that a particle at that site travels during a single cardiac cycle, defined as,

$$\mathrm{RRT} \sim \left(\frac{1 - 2 \times \mathrm{OSI}}{T}\int_0^T |\boldsymbol{\tau}_w| dt\right)^{-1}$$

The expression on the right is used as the indicator of RRT to represent the average amount of time that a particle spent in a specific region.

2.4. Compact stent model construction and analysis

The deployment of multiple stents forms cross-stent 3D structures (Fig. 4A). To investigate the influence of multi-layer structures, a compact model with a single layer was built for comparison. In cases with more than one stent, upon the solid-solid interaction completion, the geometry of each inner stent was projected outwards to the surface of the first stent and merged as a single stent. An artificial stent with the same merged configuration was created to mimic the cases with two, three and four stents, respectively (Fig. 4B) to keep the porosity identical. The radius and length of the artificial stent were the same as the real stent. One-way FSI was performed to quantify the change of local haemodynamic environment modulated by each compact stent and compared with the corresponding MOUS system.

3. Results

3.1. Porosity

Four stents were deployed for this patient in order to achieve sufficient flow reduction based on digital subtract angiology (DSA) according to surgeons' experiences (Fig. 5). The deformed configuration of each stent was reconstructed from the post-operative CTA images and the porosity after each deployment was calculated. The porosity of one single stent is 83%, indicating stent struts covered 17% area of the corresponding cylinder surface. The subsequently deployed stents decreased the overall porosity (Fig. 4C&D), with the 2nd, 3rd and 4th stents deployment reduced the porosity to 69%, 56% and 46%, respectively (Fig. 4D).

3.2. Velocity, shear stress, oscillatory shear index, and particle relative resident time

The flow-diverting effect can be assessed according to the difference between the pre- and post-operative signal intensity (Fig. 5). The difference in velocity, shear stress, OSI, and RRT in the sac was analysed. The sac region was defined by the volume enclosed by the stent and sac wall with the following steps: (1) a convex hull was used to enclose the deployed stents; (2) the intercepts between the hull and arterial wall were calculated. Values at the node in the volume enclosed by the hull and the arterial wall including sac were extracted for analysis.

Quantitative comparisons of velocity were shown in Fig. 6. After the 1st stent was deployed, the mean sac time-averaged velocity decreased from 39.8 mm/s to 25.3 mm/s (36.4% reduction). The deployment of 2nd, 3rd and 4th stents further reduced the velocity to 20.2 mm/s (49.3% reduction), 16.0 mm/s (59.8% reduction) and 14.8 mm/s (62.8% reduction), respectively. The relationship between the reduction rate and porosity was: reduction rate = -0.658 porosity^2-0.368 porosity+1.013 with the consideration that: if the porosity is 100% (no deployment) the rate reduction is 0% and if the porosity is 0% (total occlusion) the reduction rate is 100%.

Associated with changes of flow velocity, the mean TAWSS on the sac inner surface decreased from 0.19 Pa to 0.15 Pa when the 1st stent was deployed, and further decreased to 0.13 Pa after subsequent stents were deployed (Fig. 7A). The flow became more disturbed after the 1st stent was deployed as OSI increased from 0.18 to 0.30, and the deployment of the subsequent stents further increased OSI to 0.40 (2nd stent), 0.44 (3rd stent) and 0.44 (4th stent), respectively (Fig. 7B).

RRT at the proximal disease-free region where the flow fully developed was 8.5 Pa^{-1}, and it changed to be 8.4 Pa^{-1} after the first stent was deployed, while remained nearly unchanged after subsequent stents deployment (Fig. 7C). When the first stent was deployed, the mean $\overline{RRT}$ on the sac inner surface increased from 1.29 to 3.13; it further increased to 4.90 (2nd stent), 17.78 (3rd stent) and 18.80 (4th stent). The mean time-averaged pressure in the sac decreased by 2.4% after the first stent was deployed, and decreased further by 4.2% (2nd stent), 5.4% (3rd stent) and 5.6% (4th stent) when the subsequent stents were deployed.

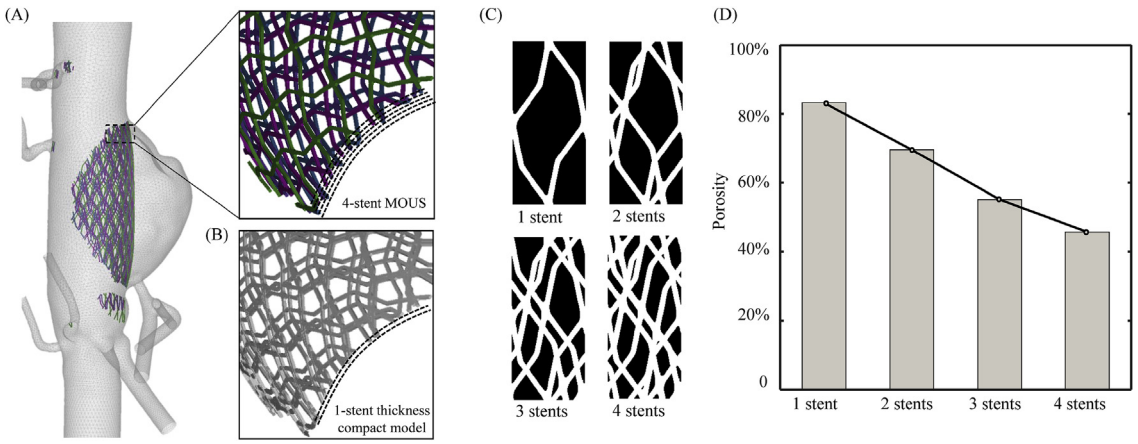

Fig. 4. The 3D structure of a 4-stent MOUS and the corresponding compact model. (A) The configuration of MOUS with a local view and lumen surface after the deployment of 4 stents. The four stents were in different colours, while stent struts contacting the wall were masked out; (B) The local view of corresponding compact model; (C) A unit cell of the projection of 1 stent, 2 stents, 3 stents and 4 stents, respectively; (D) Corresponding porosity calculated from the relative area ratio of the stent struts.

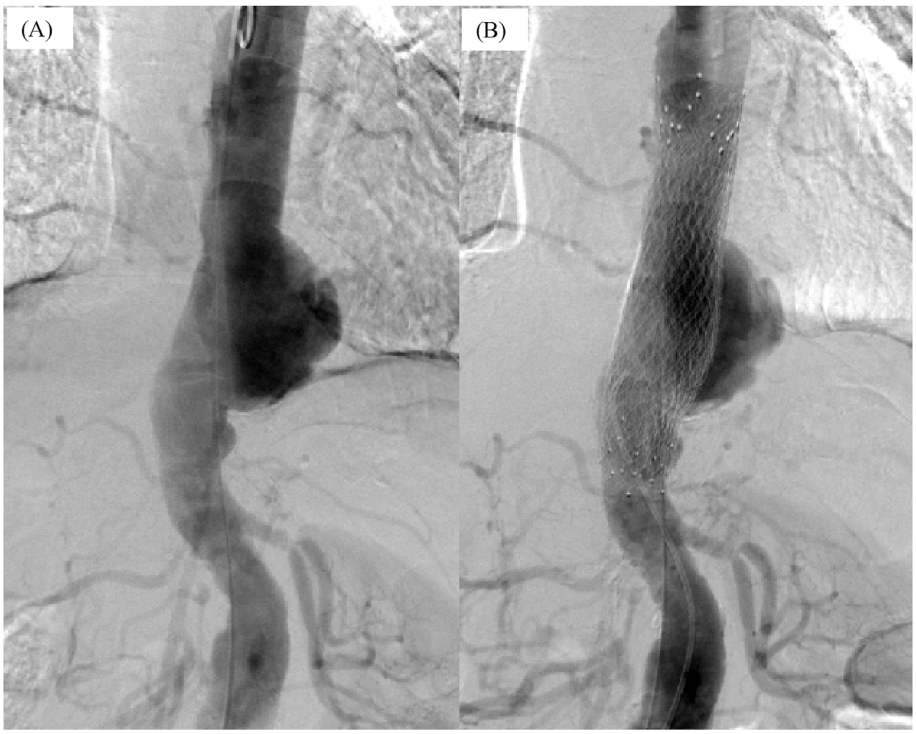

Fig. 5. The digital subtract angiology (DSA) prior to and after MOUS deployment.

3.3. The change of velocity, shear stress, oscillatory shear index, and particle relative resident time in the compact model

Similar to the multi-layer MOUS, the single-layer compact models modulated the flow pattern and decreased the flow velocity inside the aneurysm sac (Fig. 6B&C). After the deployment of 2-stent MOUS, the mean sac-averaged velocity was 20.2 mm/s, and the corresponding 2-stent compact model yielded a similar mean velocity of 19.9 mm/s (Fig. 6B), the flow velocity of 3-stent MOUS and compact model were 16.0 mm/s and 15.2 mm/s, respectively, and 14.8 vs 13.7 mm/s for 4 stents (Fig. 6B&C). The difference of other haemodynamic variables including, TAWSS, OSI and $\overline{RRT}$, between the MOUS and corresponding compact model was all less than <5% as listed in Table 1. The mean time-averaged pressure in the sac between MOUS and corresponding compact models were equivalent (relative difference <1%).

3.4. Vessel structural stress (VSS) modulated by stents

Right after the first stent was deployed, the aneurysm configuration changed immediately due to the solid-solid interaction, and VSS increased accordingly depending on the location. The change of stress of the representative node in different regions was shown in Fig. 8. When the first stent was deployed, at points in direct contact with the stent struts, particularly in the landing zone, the stress level could increase over 5 times (Fig. 8, Nodes B&D). The stress increased more gently in the non-contact points, e.g., VSS could be doubled in the non-contact landing zone (Fig. 8, Node A); however, the value in the sac remained nearly unchanged (Fig. 8, Node C). In summary, the peak stress around the

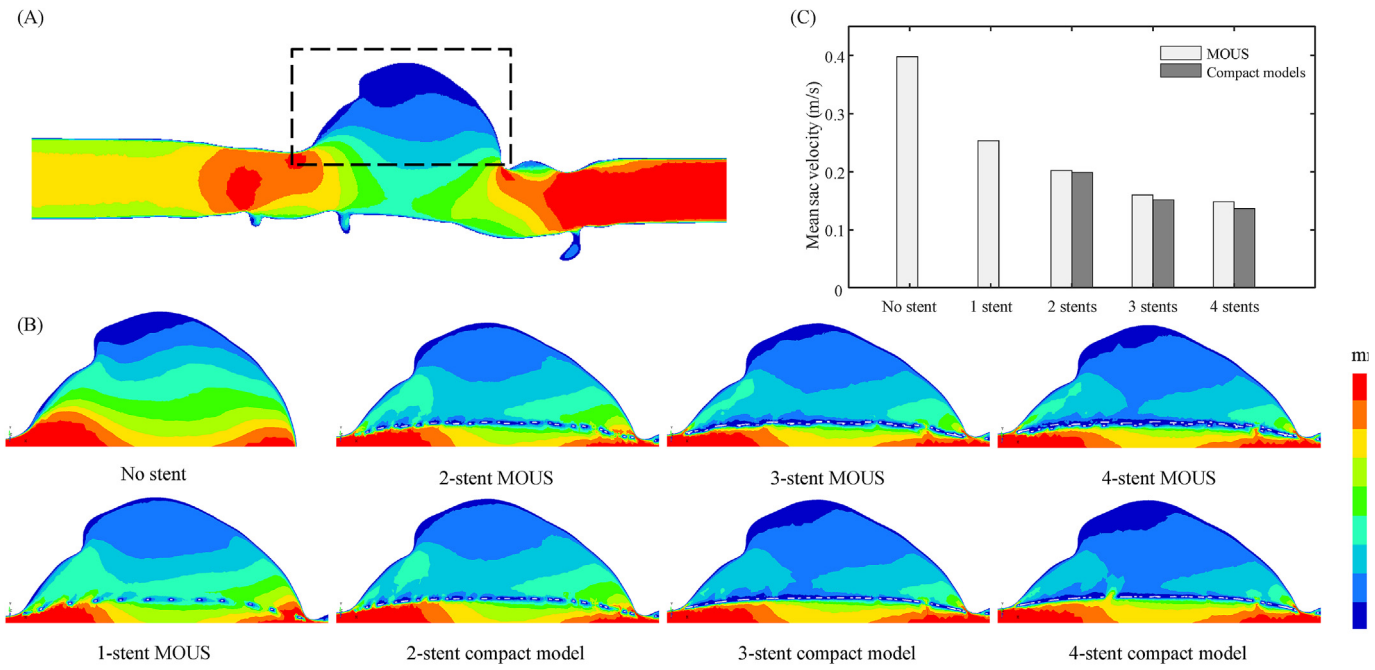

Fig. 6. Comparison of velocity reduction between the MOUS and compact models. (A) Cross-sectional band plot of velocity without stent deployment at systole; (B) The local view of the flow velocity in the aneurysm sac before and after the deployment of MOUS and corresponding compact models; (C) Quantitative comparison of the mean sac velocity between MOUS and corresponding compact models.

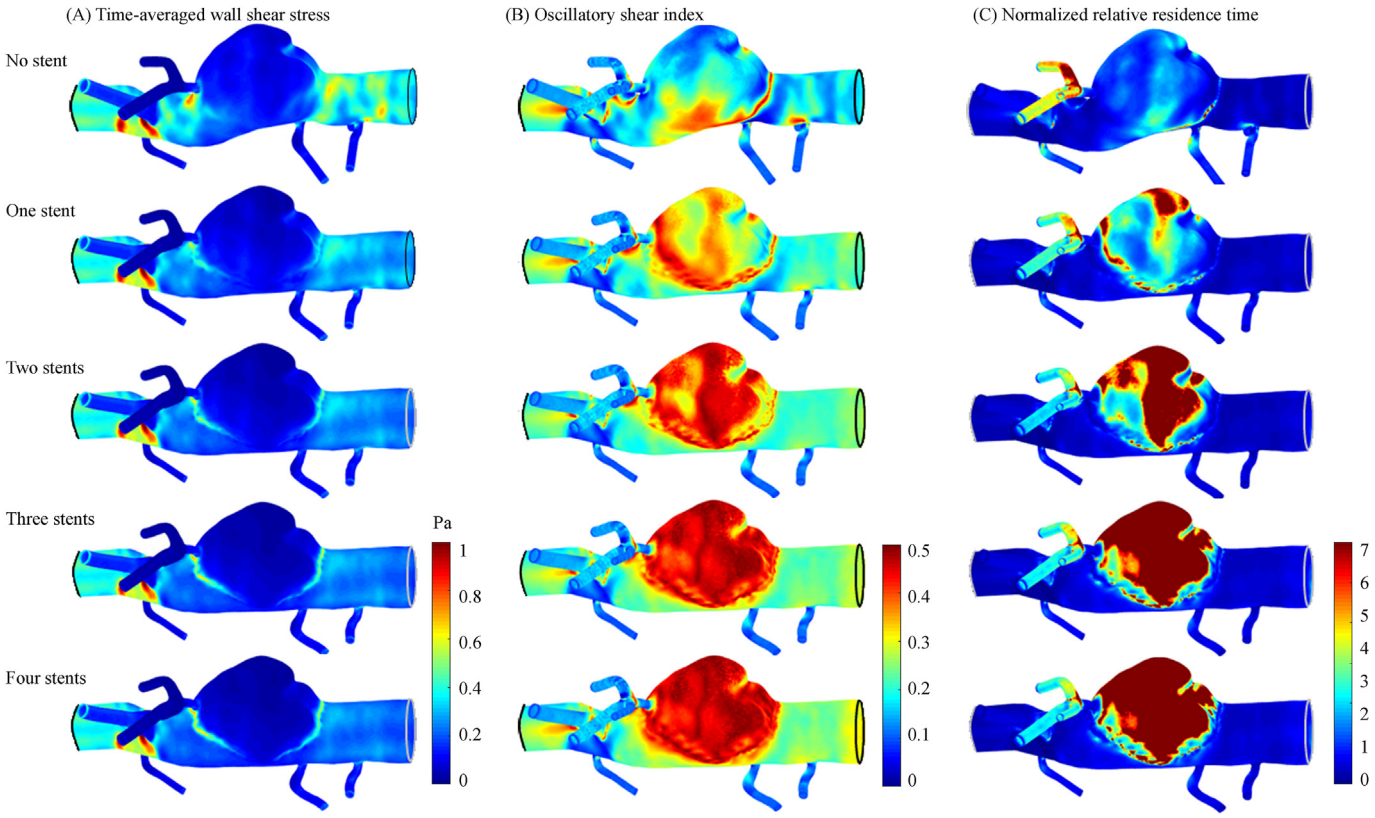

Fig. 7. Comparison of time-averaged wall shear stress (TAWSS), oscillatory shear stress (OSI) and normalised particle relative residence time ($\overline{RRT}$) in models without and with different number of stents (A: TAWSS; B: OSI and C: $\overline{RRT}$).

diseased region could increase 12 times from 143 kPa to 1718 kPa after 4 stents were deployed and such stress elevation was only observed in the landing zone, not in the aneurysm sac.

The VSS level after the deployment of corresponding compact models was lower than MOUS, while varied on the different locations (Fig. 8). In this study, the 2-stent compact model induced a peak structural stress

Table 1
Comparison of haemodyamic variables averaged on the aneurysm wall, between MOUS and corresponding compact models.

Variables	2-stent		3-stent		4-stent	
	MOUS	Compact model	MOUS	Compact model	MOUS	Compact model
TAWSS (Pa)	0.14	0.14	0.13	0.13	0.13	0.12
OSI	0.40	0.40	0.44	0.43	0.44	0.44
$\overline{\mathbf{RRT}}$	4.90	4.82	17.77	17.79	18.80	18.91

about 14% lower than 2-stent MOUS, while VSS within the sac wall (Fig. 8, Node C) was about 6% lower. Similarly, after the virtual deployment of 3-stents compact models, the peak structural stress and sac VSS were about 12% and 18% lower than MOUS, respectively. The 4-stent compact model reduced the peak stress level about 14%, and 23% in the sac wall, compared to the 4-stent MOUS.

4. Discussion

This study demonstrated that the porosity is a key determinant of the flow-diverting effect, whilst the 3D cross-stent configuration plays a minor role as shown by a small difference in local haemodynamic parameters between MOUS model and corresponding compact models.

The reduction of flow velocity and increased RRT/$\overline{\text{RRT}}$ on the sac inner surface promote the formation and development of thrombus [10]. However, the optimal number of stents remains unclear. The porosity decreases with the number of stents (Fig. 4F). Using the same stent, Shuo et al. performed a virtual random deployment following a Monte Carlo procedure [13]. Results obtained showed that when the second stent was deployed the porosity reduced by 14% (from 69.3% to 83.2%), while the third and fourth stent led to a further reduction of overall porosity by 12% and 9%, respectively. It is obvious that flow velocity reduces when MOUS is deployed. However, the efficiency of flow velocity reduction diminishes with the number of stents increases (Fig. 6C) and $\overline{\text{RRT}}$ remains nearly unchanged when the 4th stent is deployed. In this study $\overline{\text{RRT}}$ was 17.78 when the 3rd stent was deployed and 18.80 when the 4th stent was deployed and OSI remained unchanged with the 4th deployment. In a clinical study with 40 patients, 3.3 stents were deployed. These suggest that 3-stent MOUS might be optimal for managing complex aortic aneurysm.

The 3D multi-layer MOUS did not show better performance on the flow-diverting outcome compared to the corresponding single-layer structure (Table 1). Instead, a further small velocity reduction was observed in the 3-stent and 4-stent compact models than MOUS (Fig. 6). This could be explained by the elimination of 3D 'tunnels' across the dimension of thickness, during the projection of multiple layers to single-layer structure, which reduced the effective porosity.

As shown in Fig. 8, more stents introduce higher VSS concentrations in the diseased region, particularly at the landing zones (Fig. 8). Prior to the first deployment, the peak stress around the diseased region was 143 kPa, it increased linearly to 1718 kPa, when the 4th deployment was made. The compact model reduces the overall stress level by 10%–20%. Such high structural stress concentrations within landing zones after MOUS deployment might have undesirable effects, such as continued tissue degeneration of the aortic wall [28,29]. After two stents or the equivalent compact stent were deployed, the mean sac velocity reduced by ~50% and the peak structural stress was about 1000 kPa. If a third stent was added, the mean sac velocity reduced by ~60%, and the peak structural stress increased to ~1200 kPa. According to direct material tests, the ultimate material strength of aneurysmal tissues was in a range of 500–2000 kPa [17,30–34]. Two or three stents could therefore be an optimal option considering the trade-off between velocity reduction and VSS concentration.

Similar with MOUS, the compact model does not decrease the pressure in the sac significantly. Since the thrombus development takes time, both MOUS and compact model are not suitable for patients with lesion in a risk of near-term rupture. Moreover, although compact models reduces the stress concentration in the diseased region, the stress concentration is still high at the landing zone. A further optimal design is

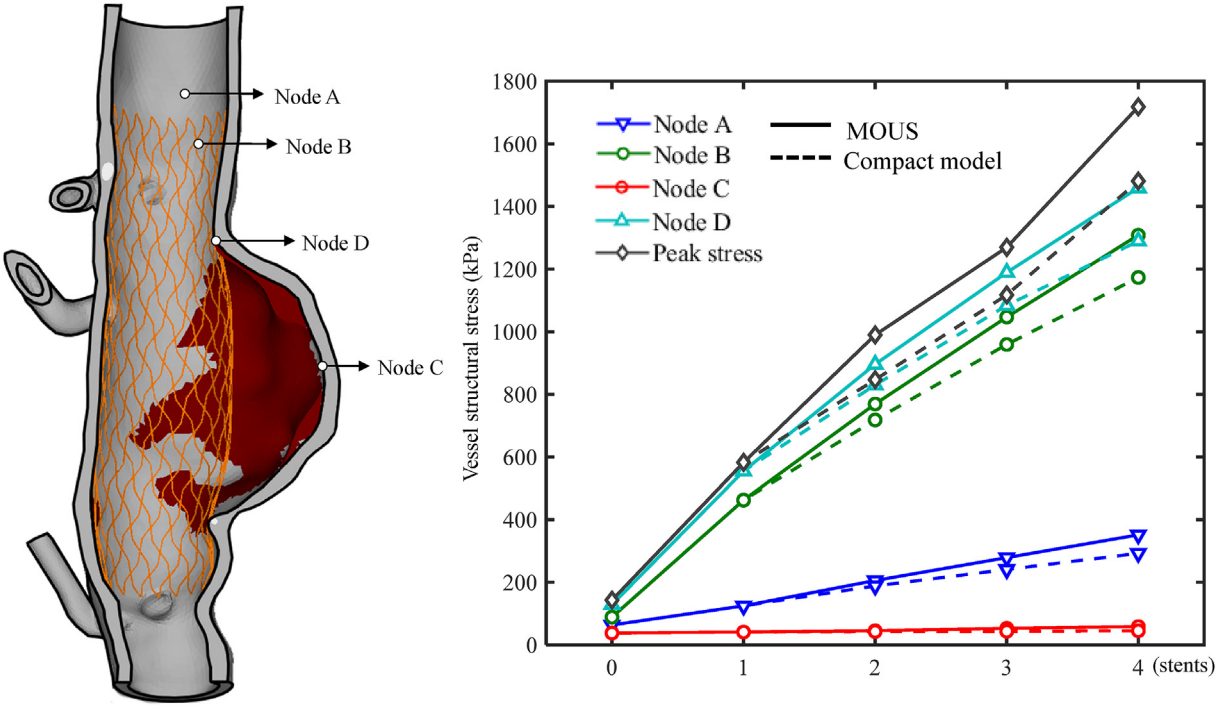

Fig. 8. Comparison of structural stress level at different location after the deployment of MOUS and corresponding compact models, with different number of stents. The results of 4 different nodes are plotted in different colours, where results from MOUS are plotted with solid line and those from compact models are plotted with dash line.

therefore required for a better treatment outcome.

In conclusion, porosity is the key determinant for the flow-diverting outcome while 3D cross-stent structures had limited influence. Better stent design with lower porosity and higher material compliance might help reduce VSS concentration and related adverse outcome. Despite the interesting findings, several limitations exist in the present study: (1) a one-way rather than fully coupled FSI analysis was performed to re-predict the mechanical environment. Due to the complexity in the geometry, interactions among aneurysmal wall, stents and blood flow, the non-linearity in material properties and governing equations, as well as big deformations, it is hard to perform a fully coupled FSI analysis using current numerical methodologies. However, it has been demonstrated that a one-way FSI yielded a small deviation in predicting structural stress and flow parameters compared with those obtained from a fully coupled FSI [35]; (2) tissue components, including wall, calcium and thrombus, were assumed to be piece-wise homogenous and the inhomogeneity in each component was not considered; (3) The empirical Reynolds number for the transition to turbulence in pipe flow is 2000–2300. In this study, the Reynolds number was estimated to range from 532 to 2256 when the mean and the peak velocity of 67 mm/s and 284 mm/s were considered. The neglect of turbulence in this study should be reasonable, however, turbulent flow might still develop locally [19]; and (4) residual stress in the aneurysmal wall was not considered.

Author statement

SW and YZ collected data, perform analysis and draft the manuscript, JF collected data, YH, PH and JHG revised the manuscript significantly, and QL and ZT designed and supervised the study and revised the manuscript significantly.

Disclosure

Dr Teng is the Chief Scientist of Tenoke Ltd., UK and Nanjing Jingsan Medical Science & Technology Ltd., China. Other authors do not have any conflict of interests to disclose.

Acknowledgement

This study was supported by British Heart Foundation (PG/18/14/33562), Engineering and Physical Sciences Research Council (EP/P021654/1) and National Institute for Health Research Cambridge Biomedical Research Centre.

References

[1] Turjman F, Acevedo G, Moll T, Duquesnel J, Eloy R, Sindou M. Treatment of experimental carotid aneurysms by endoprosthesis implantation: preliminary report. Neurol Res 1993;15:181–4.
[2] Higashida RT, Smith W, Gress D, Urwin R, Dowd CF, Balousek PA, Halbach VV. Intravascular stent and endovascular coil placement for a ruptured fusiform aneurysm of the basilar artery. Case report and review of the literature. J Neurosurg 1997;87:944–9.
[3] Fiorella D, Woo HH, Albuquerque FC, Nelson PK. Definitive reconstruction of circumferential, fusiform intracranial aneurysms with the pipeline embolization device. Neurosurgery 2008;62:1115–20. discussion 1120-1.
[4] Walcott BP, Stapleton CJ, Choudhri O, Patel AB. Flow diversion for the treatment of intracranial aneurysms. JAMA Neurol 2016;73:1002–8.
[5] D'Urso PI, Lanzino G, Cloft HJ, Kallmes DF. Flow diversion for intracranial aneurysms: a review. Stroke 2011;42:2363–8.
[6] Zhang P, Sun A, Zhan F, Luan J, Deng X. Hemodynamic study of overlapping bare-metal stents intervention to aortic aneurysm. J Biomech 2014;47:3524–30.
[7] Kallmes DF, Ding YH, Dai D, Kadirvel R, Lewis DA, Cloft HJ. A second-generation, endoluminal, flow-disrupting device for treatment of saccular aneurysms. AJNR (Am J Neuroradiol) 2009;30:1153–8.
[8] Sadasivan C, Cesar L, Seong J, Rakian A, Hao Q, Tio FO, Wakhloo AK, Lieber BB. An original flow diversion device for the treatment of intracranial aneurysms: evaluation in the rabbit elastase-induced model. Stroke 2009;40:952–8.
[9] Liou TM, Li YC. Effects of stent porosity on hemodynamics in a sidewall aneurysm model. J Biomech 2008;41:1174–83.
[10] Zhang Y, Teng Z, Lu Q, Zhao Z, Bao J, Feng X, Feng R, Chen Z, Huang Y, Sadat U, Gillard JH, Jing Z. Management of complicated aortic aneurysms using multiple overlapping uncovered stents: mid-term outcome from a cohort study. Medicine (Baltim) 2014;93:e209.
[11] Zhang YX, Lu QS, Feng JX, Zhao ZQ, Bao JM, Feng R, Feng X, Jing ZP. Endovascular management of pararenal aortic aneurysms with multiple overlapping uncovered stents. J Vasc Surg 2013;58:616–23.
[12] Sfyroeras GS, Dalainas I, Giannakopoulos TG, Antonopoulos K, Kakisis JD, Liapis CD. Flow-diverting stents for the treatment of arterial aneurysms. J Vasc Surg 2012;56:839–46.
[13] Wang S, Zhang Y, Feng J, Huang Y, Tokgoz A, Sadat U, Gillard JH, Lu Q, Teng Z. Influence of overlapping pattern of multiple overlapping uncovered stents on the local mechanical environment: a patient-specific parameter study. J Biomech 2017;60:188–96.
[14] Huang Y, Teng Z, Elkhawad M, Tarkin JM, Joshi N, Boyle JR, Buscombe JR, Fryer TD, Zhang Y, Park AY, Wilkinson IB, Newby DE, Gillard JH, Rudd JH. High structural stress and presence of intraluminal thrombus predict abdominal aortic aneurysm 18F-FDG uptake: insights from biomechanics. Circ Cardiovasc Imag 2016;9.
[15] Taubin G. Curve and surface smoothing without shrinkage. 1995. p. 852–7.
[16] Raghavan ML, Ma B, Fillinger MF. Non-invasive determination of zero-pressure geometry of arterial aneurysms. Ann Biomed Eng 2006;34:1414–9.
[17] Teng Z, Feng J, Zhang Y, Huang Y, Sutcliffe MP, Brown AJ, Jing Z, Gillard JH, Lu Q. Layer- and direction-specific material properties, extreme extensibility and ultimate material strength of human abdominal aorta and aneurysm: a uniaxial extension study. Ann Biomed Eng 2015;43:2745–59.
[18] Ebenstein DM, Coughlin D, Chapman J, Li C, Pruitt LA. Nanomechanical properties of calcification, fibrous tissue, and hematoma from atherosclerotic plaques. J Biomed Mater Res A 2009;91:1028–37.
[19] Poelma C, Watton PN, Ventikos Y. Transitional flow in aneurysms and the computation of haemodynamic parameters. J R Soc Interface 2015;12.
[20] Tan FPP, Borghi A, Mohiaddin RH, Wood NB, Thom S, Xu XY. Analysis of flow patterns in a patient-specific thoracic aortic aneurysm model. Comput Struct 2009;87:680–90.
[21] Olufsen MS, Peskin CS, Kim WY, Pedersen EM, Nadim A, Larsen J. Numerical simulation and experimental validation of blood flow in arteries with structured-tree outflow conditions. Ann Biomed Eng 2000;28:1281–99.
[22] Cebral JR, Mut F, Raschi M, Scrivano E, Ceratto R, Lylyk P, Putman CM. Aneurysm rupture following treatment with flow-diverting stents: computational hemodynamics analysis of treatment. AJNR (Am J Neuroradiol) 2011;32:27–33.
[23] Murray CD. The physiological principle of minimum work : a reply. J Gen Physiol 1931;14:445.
[24] Caro CG, Fitz-Gerald JM, Schroter RC. Arterial wall shear and distribution of early atheroma in man. Nature 1969;223:1159–60.
[25] Kawaguchi T, Nishimura S, Kanamori M, Takazawa H, Omodaka S, Sato K, Maeda N, Yokoyama Y, Midorikawa H, Sasaki T, Nishijima M. Distinctive flow pattern of wall shear stress and oscillatory shear index: similarity and dissimilarity in ruptured and unruptured cerebral aneurysm blebs. J Neurosurg 2012;117:774–80.
[26] Himburg HA, Grzybowski DM, Hazel AL, LaMack JA, Li XM, Friedman MH. Spatial comparison between wall shear stress measures and porcine arterial endothelial permeability. Am J Physiol Heart Circ Physiol 2004;286:H1916–22.
[27] Sugiyama S, Niizuma K, Nakayama T, Shimizu H, Endo H, Inoue T, Fujimura M, Ohta M, Takahashi A, Tominaga T. Relative residence time prolongation in intracranial aneurysms: a possible association with atherosclerosis. Neurosurgery 2013;73:767–76.
[28] Asanuma K, Magid R, Johnson C, Nerem RM, Galis ZS. Uniaxial strain upregulates matrix-degrading enzymes produced by human vascular smooth muscle cells. Am J Physiol Heart Circ Physiol 2003;284:H1778–84.
[29] Ruddy JM, Jones JA, Stroud RE, Mukherjee R, Spinale FG, Ikonomidis JS. Differential effects of mechanical and biological stimuli on matrix metalloproteinase promoter activation in the thoracic aorta. Circulation 2009;120:S262–8.
[30] Vallabhaneni SR, Gilling-Smith GL, How TV, Carter SD, Brennan JA, Harris PL. Heterogeneity of tensile strength and matrix metalloproteinase activity in the wall of abdominal aortic aneurysms. J Endovasc Ther 2004;11:494–502.
[31] Di Martino ES, Bohra A, Vande Geest JP, Gupta N, Makaroun MS, Vorp DA. Biomechanical properties of ruptured versus electively repaired abdominal aortic aneurysm wall tissue. J Vasc Surg 2006;43:570–6. discussion 576.
[32] Mohan D, Melvin JW. Failure properties of passive human aortic tissue. I-uniaxial tension tests. J Biomech 1982;15:887–902.
[33] Reeps C, Maier A, Pelisek J, Hartl F, Grabher-Meier V, Wall WA, Essler M, Eckstein HH, Gee MW. Measuring and modeling patient-specific distributions of material properties in abdominal aortic aneurysm wall. Biomechanics Model Mechanobiol 2013;12:717–33.
[34] Vorp DA, Schiro BJ, Ehrlich MP, Juvonen TS, Ergin MA, Griffith BP. Effect of aneurysm on the tensile strength and biomechanical behavior of the ascending thoracic aorta. Ann Thorac Surg 2003;75:1210–4.
[35] Huang Y, Teng Z, Sadat U, Graves MJ, Bennett MR, Gillard JH. The influence of computational strategy on prediction of mechanical stress in carotid atherosclerotic plaques: comparison of 2D structure-only, 3D structure-only, one-way and fully coupled fluid-structure interaction analyses. J Biomech 2014;47:1465–71.